Optoelectronic support for Inertial Navigation Systems

Dawid Florczak, and Gustaw Mazurek

Abstract-Microelectromechanical systems (MEMS)-based inertial navigation units are widely utilized due to their low cost, small form factor, and low power consumption. However, they face critical limitations in high-speed rotating systems due to gyroscopic drift, saturation, and sensitivity to environmental conditions. This paper proposes a novel method for supporting inertial navigation by estimating angular velocity using ambient electromagnetic radiation detection, offering a drift-resilient and interference-immune solution.

Keywords—GNSS-denied navigation; light sensors; infrared sensors; inertial navigation; INS

I. Introduction

NE of the main challenges in navigating fast-rotating objects using inertial navigation systems (INS) equipped with MEMS sensors is accurately measuring their angular velocity. The limitations in determining this rotational speed are a primary source of errors within such systems, creating significant obstacles to improving and controlling traditional unguided rotating platforms. To overcome this issue, a novel navigation support system has been introduced. This system leverages predictive algorithms that analyze changes in environmental radiation to estimate navigation parameters during spatial movement. The miniaturization of sensors through MEMS technology has revolutionized modern navigation systems. Their growing presence in aerial and orbital platforms stems from their efficiency and adaptability [1]. However, navigation of rapidly spinning platforms remains limited by conventional gyroscopes' physical constraints, particularly regarding drift accumulation and dynamic range saturation [2].

This study focuses on developing of a cost-effective measurement platform incorporating a variety of sensors capable of detecting multiple forms of electromagnetic radiation, including visible light, infrared, and ultraviolet. Navigation data, specifically in the rotational domain, is estimated through algorithms that compute time intervals between peaks and troughs in the recorded radiation signals. To explore and validate this approach, a dedicated test stand was constructed. This setup allows for controlled experimentation across angular velocities ranging from 0 to 5400 degrees per second and variable

- D. Florczak is with Faculty of Power and Aeronautical Engineering, Warsaw University of Technology, Warsaw, Poland (e-mail: dawid.florczak@pw.edu.pl).
- G. Mazurek is with Faculty of Electronics and Information Technology, Warsaw University of Technology, Warsaw, Poland (e-mail: gustaw.mazurek@pw.edu.pl).

angles of attack between 0 and 50 degrees. The collected data serve as a foundation for developing multiple algorithms, each adapted to specific atmospheric and lighting conditions such as fog, dense cloud coverage, intense sunlight, or the transition between day and night. The ultimate goal is to identify the most effective algorithm under defined operational conditions, taking into account environmental illumination and time-of-day variations. This work introduces an innovative method to enhance inertial navigation systems, offering a unique contribution to addressing persistent issues such as MEMS gyroscope drift and saturation. The findings present a promising pathway for advancing navigation solutions for high-speed rotating objects, with systems inherently resistant to external interference or jamming.

II. LIMITATIONS OF MEMS SENSORS

MEMS gyroscopes have revolutionized inertial navigation with their compactness and low power consumption; however, they face critical limitations that hinder accurate angular velocity measurement in high-speed rotating platforms [3]. The primary challenges include limited dynamic range leading to saturation, temperature-induced drift, insufficient resolution and high noise floors, cross-axis sensitivity, and mechanical stress effects. All these factors compromise long-term stability and precision, making conventional MEMS INS unsuitable for demanding applications without additional compensation or complementary sensing methods [4].

MEMS gyroscopes typically offer measurement ranges up to 2,000–20,000°/s but operating near these limits induces non-linear behavior and output clipping, known as saturation, which corrupts angular rate estimates at high speeds. Saturation arises when the Coriolis-induced sensing element displacement exceeds the device's linear range, leading to hysteresis and gain compression. Advanced designs, such as ovenized MEMS gyros, can extend dynamic range but at the cost of increased power consumption and complexity. In practice, sensors specified for ±2,000°/s may become unreliable above $\pm 1,500^{\circ}$ /s, limiting their use in ultra-fast rotating applications. While some commercial gyroscopes, such as the ADXRS649 and ASM330LHBTR, advertise measurement ranges up to 20,000°/s, they offer insufficient sensitivity and are prone to temperature-induced errors [5].

Sensor reviews from global suppliers confirm that gyroscopes capable of withstanding high angular velocities often



D. FLORCZAK, G. MAZUREK

suffer from decreased resolution, cross-axis interference, and high thermal sensitivity [6]. These factors render them ineffective in missions demanding long-term accuracy.

III. TECHNICAL CHALLENGES

Rotating missiles introduce several obstacles for MEMS-based INS systems:

- Gyroscopic Drift: Accumulates over time due to mechanical and thermal variances. All MEMS gyroscopes exhibit a slow, time-dependent bias instability that integrates into significant heading errors if left uncompensated. This drift stems from two primary sources:

 (a) bias instability, a near-DC wander in the sensor's zero-rate output over minutes to hours, and (b) angular random walk (ARW), a high-frequency noise component that integrates to a random drift over time. Temperature cycles exacerbate drift by altering the MEMS resonator's mechanical properties, introducing additional bias shifts that outpace standard compensation techniques [7].
- Saturation and Non-Linearity: Sensors approach their operational limits at high speeds. MEMS gyros are specified with a maximum measurement range-often between ±2,000°/s and ±20,000°/s—but approaching these limits induces non-linear gain compression and output clipping, collectively termed saturation. When Coriolisinduced displacements exceed the device's linear sensing gap, the output no longer scales proportionally with the true rotation rate, leading to gross underestimation of angular speed. Even advanced compensation algorithms can only partially correct these non-linearities at the expense of increased latency and computational burden. Practically, many "±20,000°/s" parts become unreliable beyond ±15,000°/s in real-world tests, rendering them unsuitable for ultra-fast spin measurement without additional sensing modalities [8].
- Cross-Axis Coupling: Rotational motion along multiple axes distorts primary readings. Imperfect MEMS fabrication and mechanical coupling between the X, Y, and Z sensing elements cause cross-axis sensitivity (CAS): rotation about one axis produces spurious signals on orthogonal axes. CAS levels of 0.5–2 percent full-scale are common, but when combined with centrifugal stresses in a spinning environment, these errors amplify, corrupting multi-axis attitude estimation. Calibration can reduce CAS offline, yet any shift in package stress or temperature reintroduces coupling errors, necessitating frequent recalibration for high-accuracy applications [9].
- Centrifugal Effects: MEMS sensors operating at high angular velocities are subjected to significant centrifugal forces, which can induce mechanical stress or deformation in sensing elements. This physical strain may alter the sensor's intrinsic properties, degrading measurement accuracy and increasing cumulative errors in the inertial navigation system. [10].
- Environmental Vulnerability: Thermal and mechanical stresses exacerbate inaccuracies. High rotational speeds impart strong centrifugal and vibrational forces on the

MEMS structure, deforming the resonator and shifting its natural frequency. This mechanical stress alters the scale factor and increases noise, especially when resonant elements experience fatigue over repeated cycles. Furthermore, MEMS gyros are highly temperature-sensitive; thermal expansion of silicon alters beam stiffness and damping, causing bias shifts of hundreds of °/h per °C if uncompensated. Rapid temperature transients—common in aerodynamic heating—can outpace on-chip compensation loops, producing transient errors that degrade navigation performance [11].

Moreover, attempts to replace or augment gyroscopes with off-axis accelerometers suffer their own drawbacks. While an accelerometer mounted at a known radius can infer angular rate from centrifugal acceleration, these devices exhibit even larger temperature coefficients, lower bandwidth, and require complex multi-sensor fusion algorithms (e.g., extended Kalman filters) that demand high computational power and rigorous calibration, further increasing system cost and power consumption [12].

IV. VULNERABILITY OF GNSS-BASED SYSTEMS

GNSS satellites broadcast signals at power levels around 25 W, which, after traveling 20,000 km, arrive at receivers with noise-level signal strength, rendering them easy to jam even with the modest ground-based emitters. Because GNSS signals are unencrypted and predictable, adversaries can also generate counterfeit or noise waveforms to mask genuine satellite transmissions, causing receivers to lose lock or compute erroneous positions. Jamming of GNSS not only disrupts positioning and timing for civil users but also degrades synchronization in power grids, telecommunications networks, and financial systems that depend on precise GNSS timing [13] [14].

Murmansk-BN is a strategic, vehicle-mounted EW system introduced into Russian service in 2014 to provide broadarea HF and GNSS signal denial. Each Murmansk-BN battery comprises multiple KamAZ trucks equipped with telescoping antenna masts up to 32 m high, forming a networked jamming array capable of covering areas up to 640,000 km². Russian sources claim the system can jam signals at ranges between 5,000 and 8,000 km, effectively blanketing entire regions such as the Black Sea, Eastern Europe, or the Baltic states. Murmansk-BN targets satellite navigation bands (L1, L2, L5) as well as high-frequency military communications, using broad-spectrum noise and deceptive techniques to overwhelm receivers.

Commercial and military platforms relying exclusively on GNSS—such as autonomous vehicles, precision-guided missiles, and maritime navigation—can experience total loss of situational awareness when subject to Murmansk-BN jamming.

These challenges illustrate why reliance on GNSS alone is increasingly untenable in high-risk scenarios. Strategic EW assets like Murmansk-BN underscore the need for robust, multilayered navigation architectures that blend INS augmentation, terrestrial aids, and anti-jamming technologies to maintain operational continuity under electronic attack.

V. PROPOSED OPTOELECTRONIC SUPPORT FOR NAVIGATION

The proposed navigation augmentation system bypasses reliance on traditional inertial or satellite data. Instead, it uses multiple sensors detecting visible, infrared, and ultraviolet light. The system can estimate angular velocity by analyzing periodic changes in radiation levels during rotation.

Each full rotation yields identifiable radiation maxima and minima. Algorithms calculate the period between these extrema to estimate angular speed. This approach offers a low-cost, passive alternative to mitigate drift, improve resilience, and maintain navigational integrity in environments where conventional systems fail.

The hardware construction of optoelectronic support for inertial navigation consists of the following parts, as shown in Fig. 1:

- Array of light sensors,
- Analog front-end,
- Digital signal processing block.

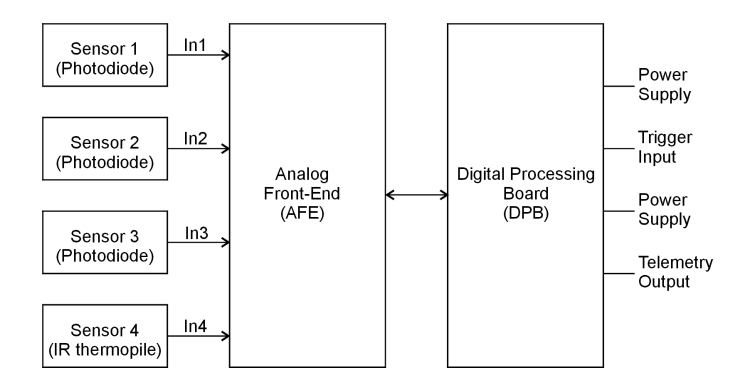
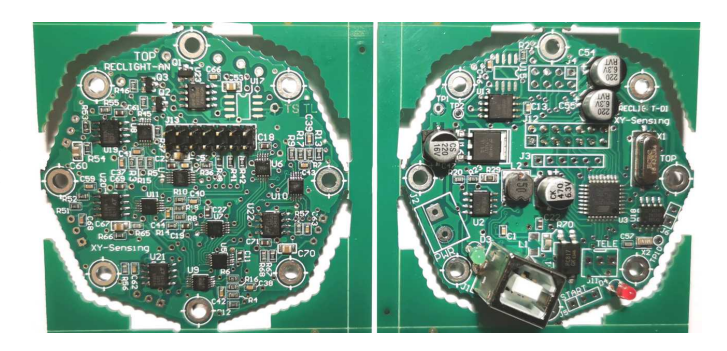


Fig. 1. Block diagram of the device

Four light sensors are connected to the device, each operating in a different spectral range. Three sensors (for visible and UV light) are photodiodes, and the IR sensor is in the form of a thermopile. Therefore, the IR sensor needs different analog processing in an input stage of the device than the others, as described in the following Subsection. The analog and digital functionalities have been physically divided into separate printed circuit boards (PCBs) to reduce the impact of the noise from the digital parts to the sensitive analog circuits. Both PCBs are electrically connected with a two-row, 14-pin connector and assembled mechanically with spacer posts. The separate PCBs (without the sensors) are shown in Fig. 2, and the mounted device – Fig. 3.

The main functional requirements for the device are as follows:

- Four analog input channels for light sensors,
- Independent conditioning of the analog signals in each channel,
- Synchronous digitizing of the signals in four A/D converters (ADCs),
- Sampling rate: 500 Hz, ADC resolution: 16 bits,
- Real-time automatic gain control (AGC), independent in each channel,



3

Fig. 2. Analog (left) and digital (right) processing boards



Fig. 3. Assembled device (without sensors)

- FLASH storage of the acquired data and timestamps,
- Access to the acquired data via USB 2.0 port,
- DC power supply from one external source (a typical Li-Ion battery).

A. Analog front-end

An internal structure of the analog front-end board is presented in Fig. 4.

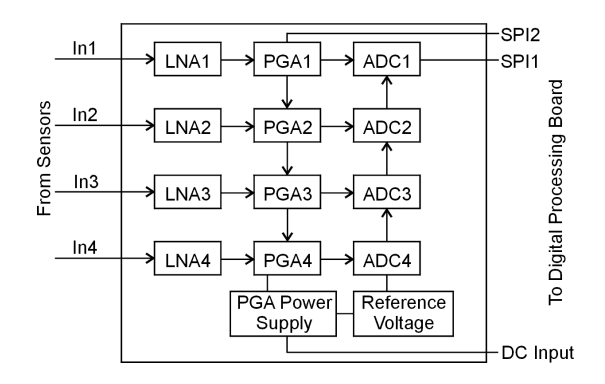


Fig. 4. Analog front-end structure

The board contains four identical analog signal processing paths, each consisting of two amplifiers followed by an

D. FLORCZAK, G. MAZUREK

Analog-to-Digital Converter (ADC) dedicated to a separate channel (and the optoelectrical sensor). These circuits are supported by a dedicated source of a reference voltage for ADC, power supply filters, and an additional power supply circuit dedicated to Programmable Gain Amplifiers (PGAs), which are required due to the internal structure of their output stages.

The signal from the optoelectrical sensor is coupled differentially with the device's dedicated analog input and fed into a Low Noise Amplifier (LNA). Depending on the sensor type, the LNA is realized either as a transconductance amplifier or a non-inverting voltage amplifier. A special low-offset and low-noise Operational Amplifier (OpAmp) has been used in both cases. The transfer characteristics of LNA for photodiodes and IR thermopiles are plotted in Figs. 5, 6, where U_{in} and I_{in} denote the input voltage and current, respectively, and U_{out} — the output voltage.

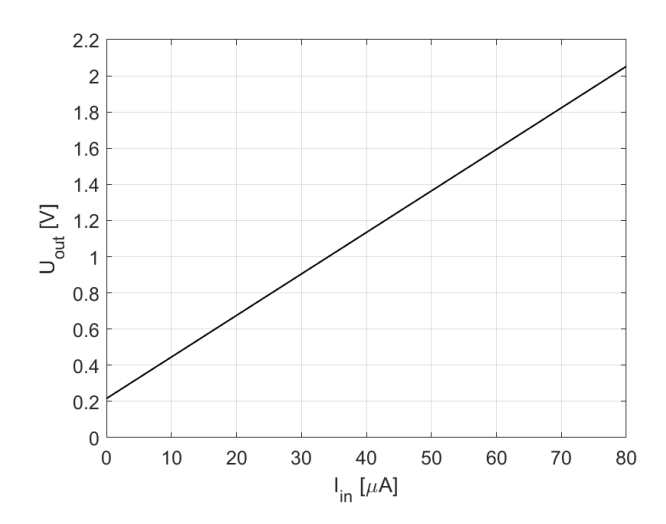


Fig. 5. Transfer function of LNA - photodiode

The OpAmps in LNA stages are also configured to perform as an active low-pass filter at the same time to suppress the high-frequency and noise components of the measured signals and to avoid the aliasing effect in ADCs.

The output voltage from each LNA is connected to the second-stage amplifier, i.e., the Programmable Gain Amplifier (PGA). The PGAs can be configured via a digital interface to independently apply one of the following voltage gain levels: 0.2,1,0,20,30,40,60,80,120,157 for each channel. The actual gain level can either be dynamically selected in the Adaptive Gain Control (AGC) algorithm launched in the embedded microcontroller or stay fixed according to the current configuration.

B. Digital Processing Board

A simplified block diagram of the Digital Processing Board is depicted in Fig. 7. The central part of this board is an 8-bit RISC microcontroller (Microchip / Atmel ATmega 328P), clocked with a crystal resonator (18.432 MHz). The first serial interface (SPI1), realized in hardware, is connected to

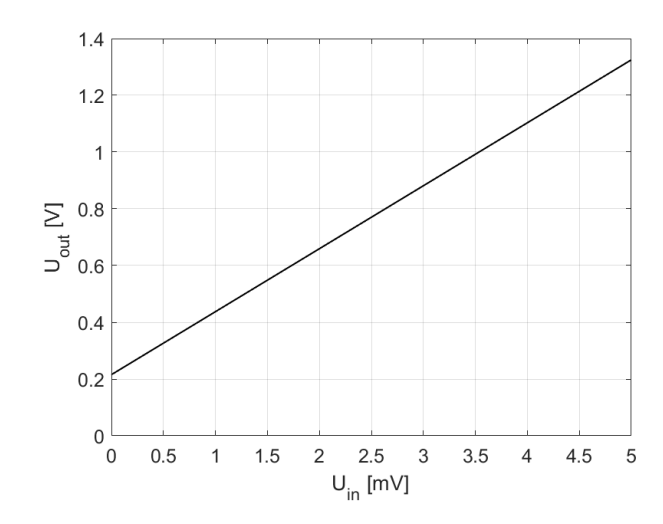


Fig. 6. Transfer function of LNA - IR sensor

an external FLASH memory (for fast storing and reading of the acquired data) and the control interface of PGAs in the Analog Processing Board. The second SPI interface (SPI2) triggers ADCs and fetches their results after completing the A/D conversion cycle. This interface is inactive most of the time (especially during the A/D conversion) to reduce the noise level in the most sensitive parts of the device. The Real-Time Clock (RTC) is responsible for counting the current date and time used to timestamp the measurement results during the data acquisition. An asynchronous UART interface is used for USB communication (via a dedicated USB bridge) during the device standby state and for sending chunks of raw data in real-time to the Telemetry Output, during data acquisition state. In the Digital Processing Board, there is also a dedicated, galvanically isolated input interface that allows the sending of a trigger impulse (a voltage signal) to MCU to start the data acquisition process. Separate power supply circuits have been implemented for analog and digital parts to reduce the noise level in the Analog Processing Board and avoid digital signals crosstalk to the sensitive analog circuits. The entire device is powered from a single DC voltage, typically from a small Li-Ion battery pack in 2S or 3S configuration.

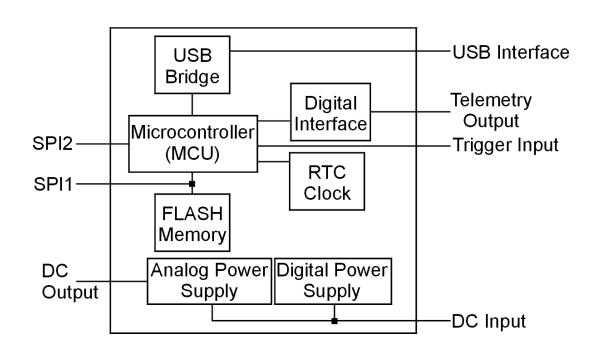


Fig. 7. Digital processing board structure

VI. EXPERIMENTAL RESULTS

Ultimately, it was assumed that the proposed technology would be tested using rapidly rotating objects, such as missiles, at a training ground. However, it was decided first to conduct laboratory tests, the results of which are presented in the two graphs below (Fig. 8 and Fig. 9). Fig. 8 presents raw data captured directly from the test setup during measurements conducted on a cloudy afternoon. The graph displays the recorded signal, representing voltage values (in millivolts) as a function of time. In the first test scenario, the setup operated at angular velocities of 360, 720, 1080, and 1440 °/s. For each velocity, tests were performed across six angles of attack ranging from 0° to 50°, increasing in 10° increments. To ensure accurate sensor data collection, each angular velocity was maintained for 6 seconds at each angle of attack. Once the maximum angle of 50° was reached, the system advanced to the next angular velocity. The tests began with an angular velocity of 360 °/s and an initial angle of attack of 0° relative to the horizontal plane on which the setup was positioned.

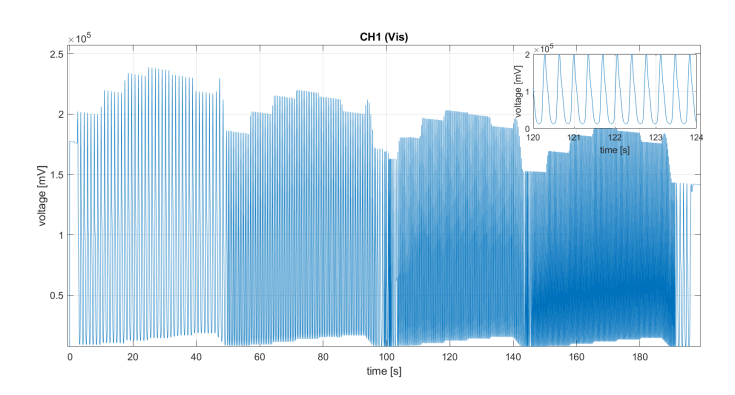


Fig. 8. Measurement results from the visible light photodiode

In the following stage, a preliminary assessment was carried out to evaluate the validity of the previously described concept. This involved analyzing the characteristics of the signals recorded from four sensors, each covering one of the targeted spectral bands—visible light, infrared, and ultraviolet radiation. Specifically, the sensors tested included:

- CH1 (Vis) GVBL-T14GD, a sensor for visible and ultraviolet radiation,
- CH2 (Vis) VTB 1013H, a sensor for visible and nearinfrared light,
- CH3 (UV) GUVA-T21GD-U, an ultraviolet radiation sensor.
- CH4 (IR) HMS M11 L3.0F8.0, an infrared sensor.

To perform this analysis, tests were conducted with the test stand operating at a linearly increasing angular velocity ranging from 0 to 3600 °/s while maintaining a constant angle of attack of 0°. Measurements were taken under two distinct lighting conditions: in bright daylight with intense sunlight and during a cloudy night.

The collected data, representing sensor output voltage (in millivolts) over time (in seconds), is displayed in graphical form. Fig. 9 illustrates the results obtained under clear sky conditions with intense sunlight at noon.

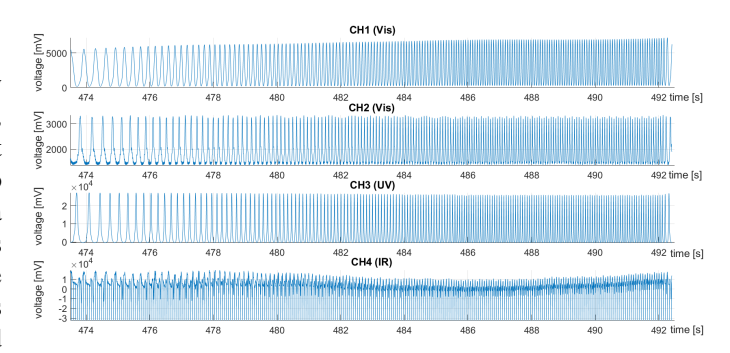


Fig. 9. Measurement results from all sensors – clear sky and high sunshine at noon.

In the next set of steps, field tests were conducted on a small-scale spinning rocket to verify the proposed concept of velocity measurement using an innovative device A view of a subsonic, rapidly spinning missile launch is shown in Fig. 10.



Fig. 10. Field testing of the proposed solution

The results are presented in Fig. 11. The blue line shows the reference values from a high-performance INS system supported by a GNSS signal. The orange line reflects the measurement results obtained using the developed system.

Angular velocities ranging from 0 to 18 revolutions per second were achieved, corresponding to an angular velocity range of 0 to 6,480 degrees per second. A good agreement between the experimental and reference (INS) values can be seen, validating the proposed optoelectronic rotation speed measurement.

VII. CONCLUSION

MEMS-based navigation systems, while versatile, struggle with long-term precision in fast-rotating applications. Using ambient light sensors provides a new, interference-proof layer

6 D. FLORCZAK, G. MAZUREK

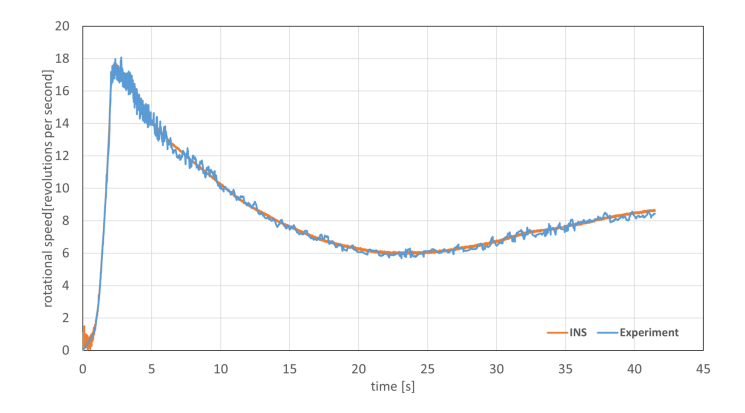


Fig. 11. Estimated angular velocity and reference from INS

of navigational data. Future work will explore integrating these systems into embedded hardware and assess their effectiveness in varying atmospheric conditions.

This navigation augmentation approach offers three significant benefits: it operates fully independent of both GNSS and gyroscope-only solutions, it is cost-effective and readily integrates with off-the-shelf INS hardware, and its simplest implementations demand only modest computational resources.

This navigation augmentation approach offers three significant benefits: it operates entirely independently of GNSS and gyroscope-only solutions, is cost-effective, and readily integrates with off-the-shelf INS hardware. Additionally, its simplest implementations demand only modest computational resources.

Together, these features enable robust, scalable deployment in GNSS-denied or jamming-prone environments, reduce system complexity and expense, and facilitate real-time operation on lightweight embedded platforms.

Moreover, it should be emphasized that the results obtained from the experiment on a small, rotating rocket and their compliance with the INS results allow us to clearly state that the proposed concept of developing a navigation system that does not use the GNNS signal support and is based on an innovative measurement of angular velocities has a high justification for further development.

REFERENCES

- [1] P. Wang, L. Lan, Y. Han, and C. Shen, "Ultra miniature mems/satellite integrated navigation system," *Lecture Notes in Electrical Engineering*, vol. 159, 2012. [Online]. Available: https://doi.org/10.1007/978-3-642-29187-6_58
- [2] D. Salgado, "An introduction to inertial navigation," An Introduction to Inertial Navigation, 2015. [Online]. Available: https://www.academia.edu/16855348/An_introduction_to_inertial_navigation
- [3] U. Nabholz, M. Curcic, J. E. Mehner, and P. Degenfeld-Schonburg, "Nonlinear dynamical system model for drive mode amplitude instabilities in mems gyroscopes," arXiv preprint arXiv:2002.02234, 2020. [Online]. Available: https://arxiv.org/abs/2002.02234
- 2020. [Online]. Available: https://arxiv.org/abs/2002.02234
 [4] X. Bu, Y. Zhang, and H. Li, "Temperature drift suppression for mems gyroscope based on vibrational-displacement control with harmonic amplitude ratio," *Micro Nano Letters*, vol. 19, no. 3, 2024. [Online]. Available: https://ietresearch.onlinelibrary.wiley.com/doi/full/10.1049/mma2.12187
- [5] M. Putnik, S. Cardanobile, C. Nagel, P. Degenfeld-Schonburg, and J. Mehner, "Simulation and modelling of the drive mode nonlinearity in mems-gyroscopes," *Procedia Engineering*, vol. 168, pp. 950–953, 12 2016.
- [6] Z. Liu and G. Han, "Resonant mems accelerometer with low cross-axis sensitivity—optimized based on bp and nsga-ii algorithms," *Microma-chines*, vol. 15, no. 8, p. 1049, 2024.
- [7] S. Dildar Ali, U. Bhatti, K. Munawwar, U. Al-Saggaf, S. Mansoor, and J. Ali, "Gyroscopic drift compensation by using low-cost sensors for improved attitude determination," *Measurement*, vol. 116, pp. 199–206, 2018.
- [8] Y. Zhao, X. Yue, F. Chen, and C. Huang, "Extension of the rotation-rate measurement range with no sensitivity loss in a cold-atom gyroscope," *Physical Review A*, vol. 104, no. 1, p. 013312, 2021.
- [9] R. Bosch GmbH, "Mems device with improved spring system," Google Patents, 2015. [Online]. Available: https://patents.google.com/patent/ US9097524B2/en
- [10] Z. Goraj and E. Cichocka, "Influence of weak and strong gyroscopic effects on light aircraft dynamics," *Aircraft Engineering and Aerospace Technology*, vol. 88, no. 5, pp. 613–622, 2016.
- [11] X. Ru, N. Gu, H. Shang, and H. Zhang, "Mems inertial sensor calibration technology: current status and future trends," *Micromachines*, vol. 13, no. 6, p. 879, 2022.
- [12] J. B. Bancroft and G. Lachapelle, "Data fusion algorithms for multiple inertial measurement units," *Sensors*, vol. 11, no. 7, pp. 6771–6798, 2011
- [13] E. Axell, F. M. Eklöf, P. Johansson, M. Alexandersson, and D. M. Akos, "Jamming detection in gnss receivers: Performance evaluation of field trials," *NAVIGATION*, vol. 62, no. 1, 2015. [Online]. Available: https://doi.org/10.1002/navi.74
- [14] T. Morong, P. Puričer, and P. Kovář, "Study of the gnss jamming in real environment," *International Journal of Electronics and Telecommunications*, vol. 65, no. 1, 2019. [Online]. Available: https://doi.org/10.24425/ijet.2019.126284